Bayesian Analysis of the Nexus Paradigm Predictions for Supermassive Black Hole Observations by the Event Horizon Telescope

Stuart Marongwe *, Moletlanyi Tshipa, Christian Corda

Posted Date: 25 July 2025

doi: 10.20944/preprints202507.2095.v1

Keywords: EHT observations; quantum gravity phenomenology; general relativity; black hole physics

 doi:10.20944/preprints202507.2095.v1

Article

Bayesian Analysis of the Nexus Paradigm Predictions for Supermassive Black Hole Observations by the Event Horizon Telescope

Stuart Marongwe [1,*] and Moletlanyi Tshipa [1] Christian Corda [2]

[1] Physics Department, University of Botswana

[2] SUNY Polytechnic Institute, New York, USA

* Correspondence: stuartmarongwe@gmail.com

Abstract

We present a Bayesian statistical analysis to evaluate the Nexus Paradigm (NP) of quantum gravity, as proposed by Marongwe (2023), using horizon-scale observations of supermassive black holes (SMBHs) Sagittarius A* (Sgr A*) and M87* from the Event Horizon Telescope (EHT). The NP predicts angular diameters for the dark depression, emission ring, and base diameter, which we compare to EHT measurements. Employing Gaussian likelihoods and priors informed by mass-to-distance ratio uncertainties, we compute the posterior distribution for the angular scale parameter θ_g,achieving a combined $\chi^2 \approx 0.0062$ (four degrees of freedom) corresponding to a 4.37σ (99.9972%) confidence level. Individual features show deviations $< 0.1\sigma$ supporting the NP's claim of 99th percentile agreement. Compared to General Relativity (GR), which predicts a shadow diameter inconsistent with the observed dark depression ($\chi^2 \approx 168, \sim 12.97\sigma$) the NP is favoured with a Bayes factor of $\sim 10^{36}$. These results validate the NP's predictions and highlight its potential as a quantum gravity framework, though refined uncertainties and broader model comparisons are recommended.

Keywords: EHT observations; quantum gravity phenomenology; general relativity; black hole physics

1. Introduction

Black holes (BHs) provide a unique laboratory for testing theories of gravity in the strong-field regime, where quantum effects may become observable. The Event Horizon Telescope (EHT), using Very Long Baseline Interferometry (VLBI), has produced horizon-scale images of the supermassive black holes (SMBHs) Sgr A* and M87*, revealing features such as a central dark depression, a bright emission ring, and a base diameter [1–11]. These observations, with angular resolutions as fine as 19 μas, offer a unique opportunity to test GR against alternative gravity models, exotic compact objects (e.g., wormholes, naked singularities), and quantum gravity frameworks. The current literature uses EHT data to analyze shadow size, shape, and emission properties, constraining deviations from GR. It often combines this with GRMHD simulations to model accretion flows.

In this work, we re-examine the work by Marongwe [12] in which the Nexus Paradigm (NP), a lattice gauge theory of quantum gravity in Clifford space, which models spacetime as a quantized crystal with 10^{60} eigenstates [12–14] claims a "99th percentile confidence interval" agreement with EHT data, but lacks detailed statistical analysis. The NP predicts distinct BH properties, including a halved Schwarzschild radius$r_g = r_s/2$ and quantized orbital speeds $v_n = c/n$ leading to specific angular diameters for SMBH features.

This paper conducts a Bayesian statistical analysis to rigorously test NP predictions against EHT observations for Sgr A* and M87*. We compute the posterior distribution for the angular scale parameter θ_g, assess goodness of fit using the χ^2 statistic, and compare NP to GR. Our results

 doi:10.20944/preprints202507.2095.v1

quantify the NP's consistency with observations in terms of sigma confidence levels, validating its claims and highlighting its advantages over GR.

The paper is organized as follows. In Sec. 1 we discuss the methodologies for testing gravity theories using the EHT observations. This section allows a broad understanding of testing gravity using EHT observations. We examine key studies in this regard taking into consideration their focus, findings and significance. We then investigate their limitations and challenges as well as future directions. In Sec. 2 we give an overview of the fundamental physics of the Nexus Paradigm (NP); its semi-classical version and in its full canonical quantized form. In Sec. 3 we outline the predictions of the Nexus paradigm. In Sec. 4 we discuss the data from the EHT observations. In Sec. 5 we implement the Bayesian analysis and in Sec. 6 we report the results of the analysis and draw concluding remarks and outline future directions.

1.1. Methodologies for Testing Gravity Theories

The primary methodology in the current literature involves comparing the observed black hole shadow size and shape with theoretical predictions from GR and alternative models. The shadow size is determined by the photon sphere, which depends on the spacetime metric, making it a sensitive probe for deviations from the Schwarzschild or Kerr solutions. Key approaches include:

Shadow Size Measurements: In which studies use the angular diameter of the shadow, calibrated by the mass-to-distance ratio of the black hole, to test theoretical models.

Parameterized Metrics: These are used to test deviations from GR. These include the Rezzolla-Zhidenko framework [15] or the parameterized Schwarzschild metric (PSM) proposed by Tian & Zhu [16]. These metrics introduce free parameters to model deviations from GR, which are then constrained by EHT data.

GRMHD Simulations: Since in GR the shadow is surrounded by emission from accreting matter, GRMHD simulations are used to model the observed ring and distinguish between gravitational and astrophysical effects[6–10,17]

Alternative Gravity Models and Exotic Objects: Here, studies test specific alternative theories (e.g., Einstein-Æther, quadratic gravity, mimetic gravity) and compact objects like wormholes or naked singularities by computing their shadow properties and comparing them to EHT observations[17,18]

1.2. Key Studies and Findings

The literature spans a range of gravity theories and compact objects, with EHT observations providing stringent constraints. In this section we summarise some pivotal studies. We examine their focus, findings and significance. One of the highly cited studies in this regard is the work by Vagnozzi et al. [17]. This work focuses on a comprehensive study to test a broad array of deviations from GR using the EHT image of Sgr A*. It examines regular black holes (e.g., Bardeen, Hayward [19,20]), string-inspired spacetimes, violations of the no-hair theorem, and alternative gravity theories like beyond Horndeski models. It also tests black hole mimickers, such as the Damour-Solodukhin wormhole and naked singularities, using the shadow size and mass-to-distance ratio. The work finds that models predicting a shadow size larger than that of a Schwarzschild black hole are strongly constrained, with some constraints surpassing cosmological limits. However, certain mimickers, like wormholes, remain viable. A critique by Tsukamoto [21] notes that the Damour-Solodukhin wormhole's mass includes contributions from the parameter λ, challenging the study's assumption of $\lambda = 0$. The significance of this study lies in that it highlights the power of EHT to probe a wide range of theoretical models, though its assumptions about mass parameters require careful consideration.

Another pivotal study is by Khodadi et al. [18] which focuses on testing mimetic gravity, a modified theory related to GR via a non-invertible disformal transformation, using EHT images of M87* and Sgr A*. It examines naked singularities and black holes formed by non-trivial gluing procedures, computing their shadow properties. Khodadi et al. find that baseline mimetic gravity solutions (naked singularities and glued black holes) are inconsistent with EHT data, ruling them

 doi:10.20944/preprints202507.2095.v1

out. However, stealth Schwarzschild solutions with a trivial mimetic parameter ($\lambda = 0$) are allowed but cosmologically uninteresting. The study calls for exploring extensions of mimetic gravity. The importance of this work resides in that it demonstrates the complementarity of black hole imaging and cosmological tests in constraining modified gravity theories.

Marongwe [12] focuses on testing the Nexus Paradigm, a quantum gravity model, against EHT images of Sgr A* and M87*. It compares the predicted angular diameter of the emission ring, central dark depression, and shadow base diameter with EHT data. The work finds that the Nexus Paradigm shows excellent agreement with EHT observations at the 99th percentile credibility interval, supporting its validity in the strong-field regime. More importantly, the work provides evidence for a quantum gravity framework. Unlike many theories that focus on general shadow size, the NP provides precise angular diameter predictions for the dark depression, emission ring, and base diameter, allowing for a more granular and unique comparison with EHT data.

J.Dass et al[22] test Quadratic Gravity using the EHT observations. Quadratic Gravity is a perturbatively renormalizable quantum gravity theory. It constructs a phase space of static, spherically symmetric spacetimes, including horizonless objects and wormholes, and analyzes shadow size deviations from Schwarzschild predictions. It was found that Quadratic gravity solutions align with GR outside the photon sphere but deviate near the center. EHT data constrains these deviations, particularly through brightness within the shadow region. These findings highlight the sensitivity of shadow brightness to non-GR effects, offering a new avenue for testing quantum gravity.

Tian and Zhu [16] proposes a Parametrized Schwarzschild Metric where the event horizon is located at $r = nr_s$, with n as a free parameter to test GR deviations. It uses M87* EHT data to explore whether the event horizon's position differs from r_s. They find a value of n ≈ 2 could explain discrepancies in black hole mass measurements, suggesting possible deviations from GR in strong fields. Their work offers a simple framework for testing GR but requires further validation with Sgr A* data.

Khodadi et al. [23] tests Einstein-Æther gravity, which allows Lorentz symmetry breaking, using M87* EHT data. It calculates the photon sphere radius and shadow size for two classes of black hole solutions. They find that the shadow size is sensitive to æther parameters, and EHT data constrains these parameters, providing insights into Lorentz-violating theories. Their work demonstrates EHT's ability to test theories beyond GR that affect spacetime symmetries.

1.3. Synthesis of Findings

The literature collectively demonstrates that EHT observations are a powerful tool for testing gravity theories, particularly in the strong-field regime where GR predictions are most robust. The literature shows that models like baseline mimetic gravity and certain quadratic gravity solutions are ruled out or heavily constrained, while others, like the Nexus Paradigm , show promise. Exotic Objects that mimic black holes such as wormholes, remain viable in some cases but face challenges due to mass parameter dependencies . Findings from the literature also show that the shadow size and brightness are sensitive to spacetime geometry, but astrophysical effects (e.g., accretion) must be modelled carefully to isolate gravitational signals. In synthesis, the application of a comprehensive Bayesian analysis to evaluate the NP's consistency with observational data is a modern and robust methodological novelty in this specific theoretical testing scenario.

1.4. Limitations and Challenges

Several limitations emerge across the literature. These include Mass-to-Distance Assumptions where many studies assume the mass-to-distance ratio is independent of the gravity theory, which may not hold for alternative models. This can lead to over-constrained or invalid conclusions. Astrophysical Uncertainties also present their challenges. GRMHD simulations rely on assumptions about accretion flows, which can obscure gravitational effects. Another limitation is that while EHT's

 doi:10.20944/preprints202507.2095.v1

resolution is groundbreaking, subtle deviations from GR may require higher resolution or shorter-wavelength observations (e.g., 690 GHz).

1.5. Future Directions

The literature points to several avenues for future research. These include analysing time variability in EHT data that could probe accretion dynamics and further constrain gravity models. Including polarimetric EHT data can reveal magnetic field structures, providing additional constraints on non-GR spacetimes. Multi-Messenger Approaches which involve combining EHT data with gravitational wave observations (e.g., from LISA) could test gravity theories across different regimes . Finally, the next-generation EHT arrays or space-based VLBI could enhance sensitivity to subtle deviations from GR.

2. A synthesis of the Nexus Paradigm and its application to black hole physics

The Nexus Paradigm [12–14] is a lattice gauge theory in Clifford space where space-time is represented as a space-time crystal with 10^{60}eigenstates (see Ref.[14] for the latest version). In theNP, locations in space-time are described using local coordinates rather than points in space. These localities are displacement vectors $\Delta \boldsymbol{x} = \gamma^{\mu}\Delta x^{\mu}$characterized as quantized wave packets of space-time and can be expressed as Fourier integrals.

$$\begin{aligned} \Delta x_n^{\mu} &= \frac{2r_{HS}}{n\pi}\gamma^{\mu}\int_{-\infty}^{\infty} sinc(kx)e^{ikx}dk \\ &= \gamma^{\mu}\int_{-\infty}^{\infty} a_{nk}\varphi_{(nk\mu)}dk \end{aligned} \tag{1}$$

$$\text{Where} \quad \frac{2r_{HS}}{n\pi} = \sum_{k=-\infty}^{k=+\infty} a_{nk} \tag{2}$$

Here $\gamma^{\mu}$are the Dirac matrices, r_{HS} is the Hubble radius, $\varphi_{(nk\mu)} = sinc(kx)e^{ikx}$ are Bloch energy eigenstate functions in which the four wave vectors assume the following quantized values

$$k^{\mu} = \frac{n\pi}{r_{HS}^{\mu}} \qquad n = \pm 1, \pm 2 \ldots 10^{60} \tag{3}$$

The quantized wave packets of spacetime have a minimum four-dimensional radius equivalent to the Planck 4-length and a maximum four-dimensional radius comparable to the Hubble 4-radius. The 10^{60} eigenstates emerge from the ratio of the Hubble four radius to the Planck four length. The Bloch functions in each eigenstate of spacetime generate an infinite Bravais four lattice.

The wave packet is a compact Einstein manifold, or a trivial Ricci soliton of positive Ricci curvature of the form.

$$G_{(nk)\mu\nu} = n^2\Lambda g_{(n,k)\mu\nu} = n^2 k\rho_{\Lambda} g_{(n,k)\mu\nu} \tag{4}$$

Interestingly, there are two types of solitons; vacuum state solitons in which $n^2 = \left(\frac{r_{HS}}{r_n}\right)^2$ with a De Sitter topology and those associated with baryonic matter having an anti De Sitter topology with $n^2 = \frac{c^2 r}{GM(r)}$ .The anti-De Sitter solitons are a family of concentric black hole like spherical surfaces of radii $r_n = \frac{n^2 GM}{c^2} = n^2 r_g$ with corresponding orbital speeds of $v_n = c/n$. The innermost marginally stable circular orbit $(n = 1)$ occurs at half the Schwarzschild radius, implying that in the Nexus Paradigm, the event horizon is half the size predicted by GR. This distinctive characteristic should be observable with the Event Horizon Telescope. In contrast, the De Sitter soliton adopts low energy quantum states with an increasing radius, while the anti-De Sitter soliton adopts high energy quantum states with an increasing radius.

 doi:10.20944/preprints202507.2095.v1

In the semi-classical version of the theory, Einstein's field equations are modified to the form

$$G_{(nk)\mu\nu} = kT_{\mu\nu} + (n^2 - 1)\Lambda g_{(n,k)\mu\nu} \tag{5}$$

This form satisfies Lovelock's theorem and is formulated in De Sitter space.

The exact solution [14] in the extreme weak field is

$$\frac{d^2r}{dt^2} = \frac{GM(r)}{r^2} + H_0 v_n - \frac{H_0}{2\pi}c \tag{6}$$

Here H_0 is the value of the Hubble parameter as measured in the ground state of space-time. The metric for the vacuum state n, of the quantized space-time is of the form

$$ds^2 = -\left(1 - \left(\frac{2}{n^2}\right)\right)c^2dt^2 + \left(1 - \left(\frac{2}{n^2}\right)\right)^{-1} dr^2 + r^2(d\theta^2 + sin^2\theta d\varphi^2) \tag{7}$$

The metric equation above describes curved worldlines in flat spacetime. A notable feature of this metric is the absence of singularities. At high energies, characterized by microscopic scale wavelengths of the Nexus graviton and elevated values of n, the worldline becomes straight and the local coordinates are highly compact or localized. This characteristic also indicates asymptotic freedom in quantum gravity, as gravity (worldline curvature) diminishes asymptotically at high values of n. Consequently, at high energies, graviton-graviton interactions cease due to the lack of curvature. The worldline begins to deviate significantly from a rectilinear trajectory at low energies, where uncertainties in its location are considerable, and the associated graviton wavelengths are at macroscopic scales. In the ground state of spacetime ($n = \pm 1$) we notice that the metric signature of Eqn. (7) becomes negative and that the worldline is straight.

2.1. A Covariant Canonical Quantization of GR and a Speed of Entanglement

In the full quantum theory, GR is translated into QFT by expressing the metric coefficients in terms of the Bloch energy eigenstate functions as follows:

$$g_{(nk)\mu\nu} = \gamma_\mu \psi_{(nk)} \gamma_\nu \psi_{(nk)} \tag{8}$$

This means that the metric (geometry of spacetime), a foundational concept in GR, emerges as a composite object built from entangled Dirac spinor fields, rather than being a fundamental entity. The presence of Dirac spinors implies that spin structure (SU(2) symmetry) is built into spacetime at the most basic level. This links the quantum properties of fermions to the topology and connectivity of spacetime, offering a deeper origin for curvature and torsion. Thus geometry is quantum entanglement of spinorial modes.

From Eqn.(8) we can now express the Ricci flow for the vacuum equations as follows (note $x^0 = ict$)

$$\begin{aligned} -i\partial_t g_{(nk)\mu\nu} &= \tfrac{1}{3} c r_{HS} G_{(nk)\mu\nu} = \tfrac{1}{3} c r_{HS} (n^2 - 1)\Lambda g_{(nk)\mu\nu} \\ &= \frac{1}{3} c r_{HS} (n-1)(n+1)\Lambda g_{(nk)\mu\nu} \end{aligned} \tag{9}$$

The term on the right suggests a covariant and a contravariant derivative operating on the metric coefficient such that the Ricci flow when expressed in terms of the Bloch functions becomes

$$i\partial_t \gamma_\mu \psi_{(nk)} \gamma_\nu \psi_{(nk)} = -\frac{c r_{HS}}{12\pi^2} i\gamma_\mu \nabla^{(n-1)\mu} \psi_{(nk)} i\gamma_\nu \nabla_{(n+1)\nu} \psi_{(nk)} \tag{10}$$

where

$$\nabla^{(n-1)\mu} = \partial^{n\mu} - ik^{1\mu} \text{ and } \nabla_{(n+1)\nu} = \partial_{(n\nu)} + ik_{1\nu} \tag{11}$$

 doi:10.20944/preprints202507.2095.v1

The derivative operators on the RHS are entangled, and the coupling/diffusion coefficient, $\frac{cr_{HS}}{12\pi^2}$ is an areal speed which is the speed of entanglement with a numerical value of approximately 5.2 square parsecs per second.

The Ricci flow in the presence of baryonic matter is expressed as

$$i\partial_t\gamma_\mu\psi_{(nk)}\gamma_\nu\psi_{(nk)} = -\frac{cr_{HS}}{12\pi^2}\gamma_\mu\nabla^{(n-1)\mu}\psi_{(nk)}\gamma_\nu\nabla_{(n+1)\nu}\psi_{(nk)} + n^2H_0\gamma_\mu\psi_{(nk)}\gamma_\nu\psi_{(nk)} \tag{12}$$

where

$$n^2 = \frac{c^2r_n}{GM} = \frac{c^2}{v^2} \quad \text{and} \quad \frac{1}{3}cr_{HS}\Lambda = H_0 \tag{13}$$

Baryonic matter serves as a heat sink, while the vacuum state of space-time functions as a heat source. As a result, gravitational attraction can be described as a transfer of space-time analogous to the process by which heat moves from a source to a sink. A test particle comprised of baryonic matter (local excitations of Dirac matter fields) moves along with the space-time towards the gravitating mass.

2.2. Quantum Spatio-Temporal Dynamics

We apply Eqn. (12) to understand the behavior of space-time within the deep gravitational potential of a BH. In other words, we seek to find the quantum dynamical behavior of a reference frame in a gravitational field with reference to a stationary reference frame in the absence of gravitational field. To this end we start by reducing Eqn. (12) to the form

$$i\partial_t g_{\mu\nu} = -\frac{cr_{HS}}{12\pi^2}\frac{\partial}{\partial x^\nu}\frac{\partial}{\partial^\mu}g_{\mu\nu} + n^2H_0g_{\mu\nu} \tag{14}$$

in which the metric coefficients are expressed as follows

$$g_{\mu\nu} = \gamma_\mu\psi_{(nk)}\gamma_\nu\psi_{(nk)} = \eta_{\mu\nu}\ \psi_{(nk)}\psi_{(nk)} = \eta_{\mu\nu}g \tag{15}$$

This expression allows Eqn.(14) to be expressed in the following form after factoring out the Minkowski metric coefficient and multiplying by $\hbar$.

$$\hbar i\partial_t g = -\frac{\hbar^2}{m_G}\Box g + n^2\hbar H_0 g = -\frac{\hbar^2}{m_G}\Box g + V(r_n)g \tag{16}$$

Here the vacuum potential energy in the n-th quantum state is $V(r_n) = n^2\,\hbar\,H_0 = n^2E_0$ where $\hbar$ is the reduced Planck constant and

$$cr_{HS} = cr_{HS}\frac{\hbar}{\hbar} = \frac{c^2\hbar}{3H_0\hbar} = \frac{\hbar}{m_G} \tag{17}$$

Here $m_G = \frac{3H_0\hbar}{c^2}$ is the graviton mass implying that the graviton is a virtual particle with a range equal to the Hubble 4-radius. Equation (16) is a four-dimensional Schrödinger equation. In the absence of baryonic matter, it is analogous to the wave equation for the propagation of electromagnetic waves in a conducting medium. This analogy suggests that gravity is attenuated by the conductance of space-time, with increased attenuation at higher frequencies and energies. Additionally, Equation (17) establishes connections between macroscopic and microscopic scales, as well as between classical and quantum domains. The D'Alembertian of Equation (16) is expressed in spherical coordinates as follows:

$$\Box g = \frac{1}{r^2}\frac{\partial}{\partial r}\left(r^2\frac{\partial g}{\partial r}\right) + \frac{1}{r^2sin\theta}\frac{\partial}{\partial\theta}\left(sin\theta\frac{\partial g}{\partial\theta}\right) + \frac{1}{r^2sin\theta^2}\left(\frac{\partial^2 g}{\partial\varphi^2}\right) - \frac{1}{c^2}\frac{\partial^2}{\partial t^2} \tag{18}$$

 doi:10.20944/preprints202507.2095.v1

We then apply the method of separation of variables to solve Eqn.(16) in spherical coordinates by first expressing the function g as follows

$$g(r,t,\varphi,\theta) = R(r)T(t)Y(\varphi,\theta) = R(r)T(t)\Theta(\theta)\Phi(\varphi) \tag{19}$$

Under steady state conditions in which $-\frac{\hbar^2}{m_G c^2}\frac{d^2T}{dt^2} = -\frac{i^2E_n^2}{m_G c^2} = \frac{E_n^2}{m_G c^2}$ and $-\hbar i\partial_t T = E_n$, this methods yields the following

$$\frac{d^2\Phi}{d\varphi^2} = -m^2\Phi \tag{20}$$

$$sin\theta\frac{d}{d\theta}\left(sin\theta\frac{d\Theta}{d\theta}\right) + l(l+1)sin^2\theta\Theta = m^2\Theta \tag{21}$$

$$\frac{d}{dr}\left(r^2\frac{dR}{dr}\right) - \frac{m_G r^2}{\hbar^2}\left[V(r_n) + \frac{E_n^2}{m_G c^2} - E_n\right]R = \frac{d}{dr}\left(r^2\frac{dR}{dr}\right) - \frac{2m_G r^2}{\hbar^2}\left[\frac{V(r_n)}{2} + \frac{E_n^2}{2m_G c^2} - \frac{1}{2}E_n\right]R = l(l+1)R \tag{22}$$

where m^2 and $l(l+1)$ are constants arising from the separation of variables.

The solutions to the angular equations within the spherically symmetric confinement system are

$$\Phi_m = (2\pi)^{-1/2}e^{im\varphi} \tag{23}$$

and

$$\Theta_l^m \propto P_l^m(cos\theta) \tag{24}$$

where m is restricted to the range $-l,\dots,l$, and the associated Legendre function is $P_l^m(x) \equiv (1-x^2)^{\frac{|m|}{2}}\left(\frac{d}{dx}\right)^{|m|}P_l(x)$. Here $P_l(x)$ is the l^{th}Legendre polynomial. The product of Φ_m and Θ_l^m is the spherical harmonic

$$Y_l^m(\theta,\varphi) = \epsilon\left[\frac{(2l+1)(l-|m|)!}{4\pi(l+|m|)!}\right]^{1/2}e^{im\varphi}P_l^m(cos\theta) \tag{25}$$

where $\epsilon = (-1)^m$ for $m \geq 0$ and $\epsilon = 1$ for$m \leq 0$. The spherical harmonic is orthonormal

$$\int_0^\pi d\theta sin\theta\int_0^{2\pi}d\varphi[Y_l^m(\theta,\varphi)]^*[Y_{l'}^{m'}(\theta,\varphi)] = \delta_{ll'}\delta_{mm'} \tag{26}$$

The equation for R can be further simplified by substituting $u(r) = rR(r)$ in Eqn.(22) yielding

$$-\frac{\hbar^2}{2m_G}\frac{d^2u}{dr^2} + \left[\frac{V(r_n)}{2} + \frac{E_n^2}{2m_G c^2} - \frac{1}{2}E_n + \frac{\hbar^2}{2m_G}\frac{l(l+1)}{r^2}\right]u = 0 \tag{27}$$

This equation describes a bound quantum of space-time or a local coordinate system in an energy state E_n inside a potential $\frac{V(r_n)}{2}$ and experiencing a "centrifugal potential" $\frac{\hbar^2}{2m_G}\frac{l(l+1)}{r^2}$.

2.3. Stasis and Time Evolution

We briefly discuss time evolution on a black hole like surface $r_n = n^2GM/c^2$. On such an orbit, the kinetic energy of the system and the potential energy are in equilibrium. This yields a total energy $E_n = 0$ simplifying Eqn.(27) to the form

$$-\frac{\hbar^2}{2m_G}\frac{d^2u}{dr^2} + \left[\frac{V(r_n)}{2} + \frac{\hbar^2}{2m_G}\frac{l(l+1)}{r^2}\right]u = 0 \tag{28}$$

This generates a static state characterized by the absence of temporal evolution and baryonic matter remains in stasis. The absence of time in quantum gravity has been highlighted as one of the most difficult problems in the field [24–29]. In the NP the problem of time is resolved by introducing some instability at r_n which generates a lifetime Δt at the BH like surface determined by the

 doi:10.20944/preprints202507.2095.v1

uncertainty principle $\Delta E.\Delta t \cong \hbar$ before the system transitions to the next low energy BH like surface. The uncertainty in energy yields an uncertainty in r_n such that the surface acquires a thickness arising from $r = r_n \pm r_n/2$. When $r = r_n - r_n/2$, the BH like surface has its closest approach to a contiguous BH like surface of lower energy located at $r = r_{n-1} + \frac{r_{(n-1)}}{2}$. This allows baryonic matter to quantum tunnel from one BH like surface to the contiguous surface of lower vacuum energy state. It is now clear that metric of Eqn.(7) is describing the space-time within the thickness of a BH like surface characterized by the quantum number n. This is a semi-classical Schwarzschild like space-time and can be alternatively expressed as.

$$\Delta s_n^2 = -\left(1 - \left(\frac{2}{n^2}\right)\right)c^2(\hbar/\Delta E_n)^2 + \left(1 - \left(\frac{2}{n^2}\right)\right)^{-1}(\hbar/\Delta p_n)^2 + r^2(d\theta^2 + sin^2\theta d\varphi^2) \tag{29}$$

At high energies, the Schwarzschild space is flat and the lifetime and range within a BH like surface is short.

The quantized space is described by a series of concentric BH like surfaces or AdS Ricci solitons of radius $r_n = n^2GM/c^2$ on which no time evolution occurs as described by Eqn.(28).

Having gained insights on stasis and time evolution, we can now further simplify Eqn.(28) by making the following additional substitutions

$$\kappa_n^2 = \frac{2m_{Gn}(\frac{n^2E_0}{2} + \frac{E_n^2}{2m_Gc^2} - \frac{3}{2}E_n)}{\hbar^2} \tag{30}$$

$$\rho = \kappa_n r \tag{31}$$

Since $E_n = 0$ on a BH like surface then (30) reduces to

$$\kappa_n^2 = \frac{m_{Gn}n^2E_0}{\hbar^2} \tag{32}$$

The above expression implies

$$E_0 = \frac{1}{n^2a_0^2} \tag{33}$$

where

$$a_0^2 = \frac{m_G.}{\kappa_n^2\hbar^2} \tag{34}$$

The substitutions reduce Eqn.(28) to the form

$$\frac{d^2u}{d\rho^2} = \left[1 + \frac{l(l+1)}{\rho^2}\right]u \tag{35}$$

Thus as $\rho \to \infty$ the constant term in brackets dominates or $\frac{d^2u}{d\rho^2} \to u$, which satisfies the solution $u = Ae^{-\rho} + Be^{\rho}$. The second term is irregular as $\rho \to \infty$ implying $B = 0$ which implies $u \to Ae^{-\rho}$ as $\rho \to \infty$.

Similarly, in the reverse scenario, as $\rho \to 0$ the centrifugal potential term dominates which leads to $\frac{d^2u}{d\rho^2} \to \frac{l(l+1)}{\rho^2}u$. This condition leads to a solution $u = C\rho^{l+1} + D\rho^{-l}$. Since the second term is irregular as $\rho \to 0$ therefore $D = 0$ this implies $u = C\rho^{l+1}$ as $\rho \to 0$.

2.4. Hydrogen Like Solutions

We aim to find a solution that meets both asymptotic behaviors. We consider the ansatz $u(\rho) \equiv \rho^{l+1}e^{-\rho}v(\rho)$. A solution of this form has been solved for the simple hydrogen atom. Taking hints from Eqn.(33) and Eqn.(34), we propose that the solution to the radial equation of the quantum

 doi:10.20944/preprints202507.2095.v1

gravity system $u(\rho)$ is identical to the radial equation for the hydrogen atom. We test this proposition by comparing the expression in the quantized space for the BH like surfaces $r_n = n^2 r_g$ with that obtained from a radial function identical to that of the hydrogen atom. In this case, the radial probability distribution function is $P(r) = r^2[R_{nl}]^2$ where $R_{n,n-1}(r) \propto r^{n-1}e^{-r/nr_0}$ and will peak at a value of r determined by

$$\frac{dP(r)}{dr} = \left(2nr^{2n-1} - \frac{2}{nr_0}r^{2n}\right)e^{-2r/nr_0} = 0 \tag{36}$$

That is at $r_n = n^2 r_0$. This solution implies that $r_0 = r_g$ for the quantum gravity system characterized by an AdS Ricci soliton. Thus $v(\rho)$ is of the form

$$v(\rho) \propto L_{n-l-1}^{2l+1}(2\rho) \tag{37}$$

where $L_{q-p}^{p}(x) \equiv (-1)^p \left(\frac{d}{dx}\right)^p L_p(x)$ and $L_q(x) \equiv e^x \left(\frac{d}{dx}\right)^q (e^{-x}x^q)$ is the q^{th} Laguerre polynomial. Therefore the steady state quantum gravity system can be written as

$$g_{nlm} = A_{nl}e^{-\frac{r}{nr_g}}\left(\frac{2r}{nr_g}\right)^l L_{n-l-1}^{2l+1}\left(\frac{2r}{nr_g}\right)Y_l^m(\theta,\varphi) \tag{38}$$

where

$$A_{nl} \equiv \sqrt{\left(\frac{2}{nr_g}\right)^3 \frac{(n-l-1)!}{2n[(n+l)!]^3}} \tag{39}$$

In synthesis, the function g_{nlm} describes the quantum dynamical behavior of a local coordinate system XYZ in a gravitational potential with reference to a stationary coordinates system xyz in flat space-time. From a quantum gravity perspective, the value of r_n is not definite but uncertain relative to a stationary reference frame. The most probable value being $r_n = n^2 r_g$ as computed in Eqn.(36). The expectation value $\langle r_n \rangle$ is calculated from

$$\langle r_n \rangle = \frac{r_g}{2}[3n^2 - l(l+1)] \tag{40}$$

The function $Y_l^m(\theta,\varphi)$, describes the precession of XYZ with reference to xyz with an uncertainty in the angle of nutation (See Figure 1). This results in a fuzzy reference frame with uncertain Lorentz boosts, where only the expectation and most probable values can be calculated. It is also noted that for large distances or high energies, the wave function rapidly diminishes, indicating no discernible spatio-temporal dynamical behavior at high energies and large distances. This wobbling reference frame results in hollow conical or helicoidal astrophysical jets emerging from BHs. However, for De Sitter type Ricci solitons, the spatio-temporal dynamical behavior should be observable at large radii and low energies. Undulations in the trajectories of stars at the edges of galaxies and the enigmatic galactic planes of satellites could serve as potential indicators.

Preprints.org (www.preprints.org) | NOT PEER-REVIEWED | Posted: 25 July 2025 doi:10.20944/preprints202507.2095.v1

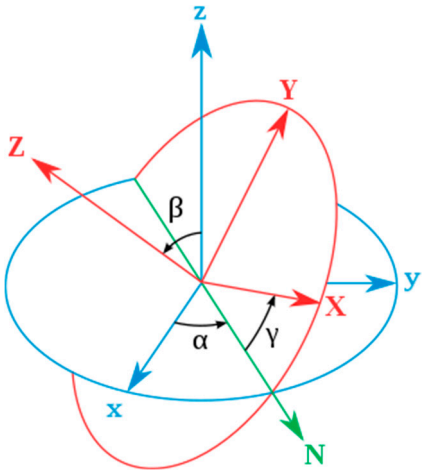

Figure 1. shows a dynamical reference XYZ frame about a stationary xyz. Image courtesy Wikipedia. $\beta =$ nutation $\alpha =$ precession $\gamma =$ intrinsic rotation.

3. Nexus Paradigm Predictions of the BH Environment

Having derived the equations governing the quantum dynamical behavior of a reference frame in a gravitational potential, we aim to predict the expected observations at horizon scales. It is essential to emphasize the key distinction between a black hole in Schwarzschild space and one in quantized space. A BH in quantized space will behave as a BH in Schwarzschild space but with half the mass. Table 1 shows how this aspect changes some important quantities associated with BHs.

Table 1.

Quantity	Schwarzschild space	Quantized Space
Schwarzschild radius	r_s	$\frac{r_s}{2} = r_g$
Photon sphere	$r_{ps} = 3r_g$	$r_{ps} = \frac{3r_g}{2}$
Impact parameter	$\boldsymbol{b = 3\sqrt{3}r_g}$	$\boldsymbol{b = \frac{3\sqrt{3}r_g}{2}}$

It is interesting to note that the photon sphere in quantized space is the expectation value of the ISCO of $n = 1$ in quantized space. That is

$$\langle r_1 \rangle = \frac{r_g}{2}[3(1)^2 - 0(0+1)] = \frac{3r_g}{2} \tag{41}$$

The innermost marginally bound orbital is computed from $r_n = n^2 r_g$ which for n=2 yields $r_n = 4r_g = 2r_s$.The expectation value for the orbital is computed as $\langle r_2 \rangle = \frac{r_g}{2}[3(2)^2 - 0(0+1)] = 6r_g = 3r_s$. The same value is obtained in GR through geometric computations, however in quantum gravity there are two sets of values. The other involves the p orbital $(n = 2, l = 1)$ which yields $5r_g = 2.5r_s$. Thus, in quantum gravity the innermost stable circular orbit can be closer than for a Schwarzschild black hole in GR.

3.1. Ray Tracing

The ray tracing in quantized space follows the same procedure as in the Schwarzschild space as computed in the literature [30,31] but having half the value of the impact parameter. Since the rays emanate from the event horizon, the rays follow a path that magnifies the image of the BH by a factor

 doi:10.20944/preprints202507.2095.v1

of $\frac{3\sqrt{3}}{2}$ such that the gravitationally lensed values for the orbits $n = 1$ and $n = 2$ will show as depicted in Figure 2. A dark central depression of angular diameter $\theta = 3\sqrt{3}\theta_g$ is to be expected. Thus for SgrA* we expect a value for the dark depression of $\theta \cong 26\ \mu$as and for M87* a value of $\theta \cong 20\ \mu$as .

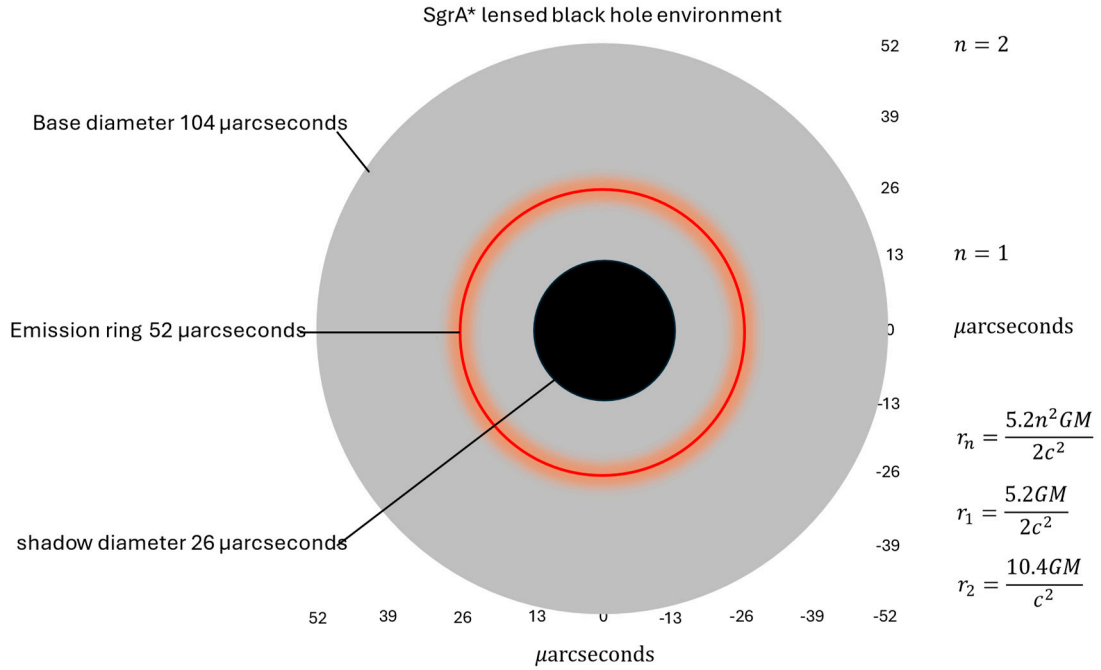

Figure 2. Shows a typical BH image in quantized space magnified by a factor of $3\sqrt{3}/2$.

4. Data and Mode

4.1. EHT Observations

The Event Horizon Telescope (EHT) observations in 2017, and prior observations from 2013, provided groundbreaking horizon-scale images of supermassive black holes (SMBHs), focusing on Sagittarius A* (Sgr A*) and M87*. Early EHT campaigns, including 2013, targeted Sgr A* using a smaller VLBI network at 1.3 mm wavelength [11,32]. The 2013 observations detected a compact source with an angular size of ~25 ± 2 μas for the central dark depression, an emission ring of ~52 ± 2 μas and a base diameter of ~104 μas [11,32]. The significance of the 2013 observations resides in that they provided initial evidence of a BH shadow, though limited by sparse baseline coverage and lower resolution. These observations were confirmed by Cho et al. [32]. The 2013 campaign faced limitations due to long-exposure-like data lacking dynamic details, and the imaging of M87* being less advanced.

The 2017 campaign expanded the EHT array to eight telescopes which included telescopes such as ALMA and SMA for improved resolution and sensitivity at 1.3 mm [2,32]. For Sgr A* the 2017 campaign, the EHT measured a dark depression of 26 ± 2 μas compared to 25 ± 2 μas in 2013. For the emission ring, the EHT measured 51.8 ± 2.6 μas (2017) compared to 52 ± 2 μas in 2013 and a base diameter of 104 μas (±3 μas). The 2019 campaign measured for M87* a dark depression of 20 μas (±2 μas), an emission ring of 40 μas (±3 μas) and a base diameter 80 μas (±3 μas). Figure 3a and Figure 3b shows the luminosity profile of M87* and the dark depression measurements of SgrA*.

 doi:10.20944/preprints202507.2095.v1

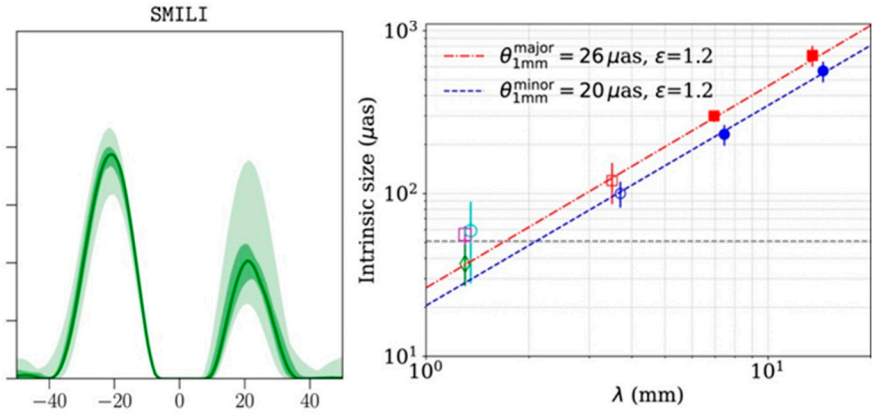

(**a**) (**b**)

Figure 3. a: Luminosity profile of M87* showing a central dark spot of approximately $20\,\mu as$ in diameter, an emission ring of approximately $40\,\mu as$ in diameter and a base diameter of approximately $80\,\mu as$ mage courtesy EHT Collaboration. **Fig 3b**: Angular diameter of the dark depression in Sgr A* as measured by Cho *et al* (2022) showing an overall size of $26\,\mu as$ The horizontal broken line (gray) shows the expected black hole shadow diameter at Sgr A* $\sim 51\,\mu as$ from GR. Image courtesy Ilje Cho *et al* 2022 *ApJ* **926** 108.

4.2. EHT Imaging Uncertainties

The observational uncertainties in the EHT 2017 (M87*) and 2019 (Sgr A*) images stem from calibration errors (gain, polarization leakage, atmospheric phase), sparse baseline coverage, algorithmic reconstruction choices, source variability (especially for Sgr A*), and astrophysical model assumptions (accretion, spin, inclination). While M87* benefited from stability and a larger angular size, Sgr A* faced challenges from rapid variability and Galactic Center interference. Ongoing improvements in telescope array size, bandwidth, and algorithms aim to reduce these uncertainties in future observations. The EHT employs 5 imaging software ,which are DIFMAP, EHT imaging, SIMILI, THEMIS and Comrade. The first 3 favour an emission ring of $40 \pm 3\,\mu as$ and later 2 favour $42 \pm 3\,\mu as$ for the 2017 campaign. We choose the size from the first three imaging software, as they are consistent with Figure 1a compared to the last two.

4.3. Nexus Paradigm Predictions

The NP predicts angular diameters based on the gravitational radius angular scale, $\theta_g = \frac{GM}{c^2 D}$, where (M) is the BH mass, (D) is the distance. The angular size of the dark depression is predicted as $\theta = 3\sqrt{3}\theta_g$in the NP. The emission ring is predicted as having an angular dimension of $\theta = 6\sqrt{3}\theta_g$ and the base diameter an angular diameter of $\theta = 12\sqrt{3}\theta_g$. Thus for Sgr A*($\theta_g = 5.02\mu$as based on $M = 4.1 \times 10^6 M_\odot$, $D = 8.0$kpc [33]) the NP predictions for the dark depression is $\theta = 25.98\,\mu$as, for the emission ring $\theta = 51.96\,\mu$as and for the base diameter $\theta = 103.92\,\mu$as. For M87*($\theta_g \approx 3.85\mu$as based on $M = 6.6 \times 10^9 M_\odot$, $D = 16.4$ Mpc [34]) the dark depression is $\theta = 19.97\,\mu$as, for the emission ring $\theta = 39.94\,\mu$as and for the base diameter $\theta = 79.88\,\mu$as. In contrast to classical General Relativity, the NP predicts that horizon scale images of black holes will appear blurry even if the EHT had infinite resolution capabilities due to significant uncertainties in location (delocalization) within regions of strong gravity [13,14]. Within the framework of the NP,the ring feature dominating BH images arises from baryonic matter quantum tunneling into the $n = 1$ orbital from the $n = 2$ orbital accompanied by radiation emission. The tunneling process peaks at a radius $r = r_n - r_n/2$,(where $r_n = n^2 r_g$) which for the $n = 2$ orbital is $r = 4r_g - 2r_g = r_s$. A gravitational lensing of the associated ring yields an angular diameter of $2 \times \frac{3\sqrt{3}}{2}\theta_s = 6\sqrt{3}\theta_g \approx 52\,\mu as$ for Sgr A*and $40\,\mu as$ for M87*. Here θ_s is the angular measurement of r_s which is equivalent to $2\theta_g$. Figure 4a and Figure 4b show the predicted base diameter, emission ring and dark depression for M87* and SgrA* by the NP.

 doi:10.20944/preprints202507.2095.v1

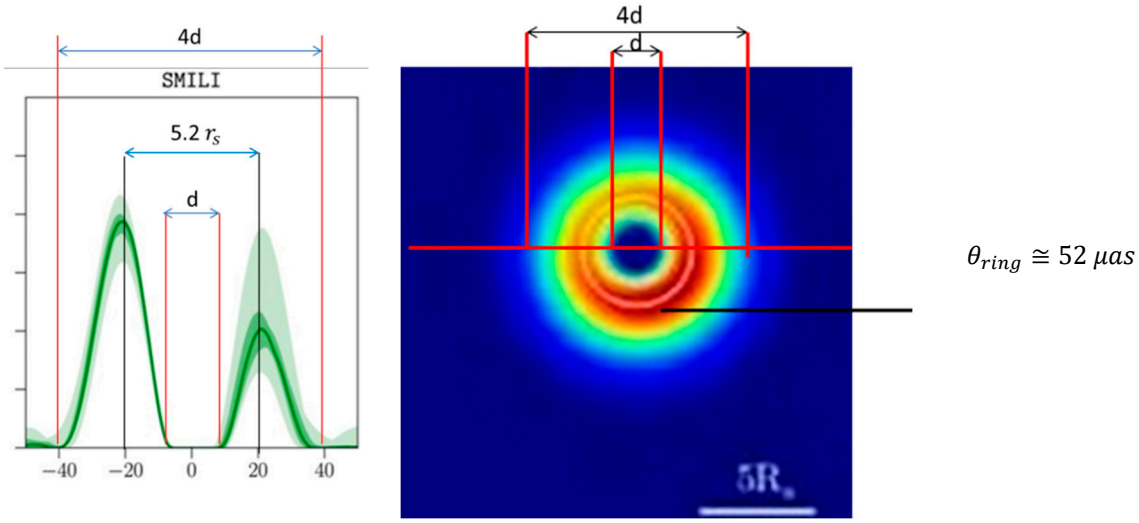

(**a**) (**b**)

Figure 4. a. The luminosity profile of M87* shows a dark depression of approximately $20\ \mu as$ with the peaks separated by $40\ \mu as$ and a base diameter of $80\ \mu as$ as predicted. Image courtesy EHT Collaboration. **b** Image of Sagittarius A* from the 2013 EHT campaign showing a central dark disk of $26\ \mu as$ in diameter and a base diameter of approximately $104\ \mu as$ and an emission ring peak of approximately $52\ \mu as$ in diameter as predicted. Image courtesy RS Lu *et al* 2018.

4.4. GR Predictions

GR predicts a BH shadow diameter of $\theta = 6\sqrt{3}\theta_g \approx 51.96\ \mu$as for SgrA*,39.94 μas for M87* which aligns with the emission ring but not the dark depression [35]. In the EHT image of M87 of 2019 or Sgr A* of 2022, the bright ring-like structure is mostly the emission ring from the accretion disk, with its brightness enhanced by gravitational lensing and Doppler effects (e.g., brighter on one side due to material moving toward the observer). There is no single, exact formula for the emission ring's size in GR because it depends on the accretion disk's physical properties, unlike the photon ring or shadow, which have well-defined sizes based on the black hole's mass and distance. The emission ring's angular size is approximately $\theta_{emission} \approx \frac{kGM}{c^2 D}$ where $k \approx 5-6$, but its breadth and exact size require numerical modeling of the accretion flow. In the EHT images, the emission ring appears as a broader, brighter feature than the photon ring, typically comparable to or slightly larger than the shadow's angular size. For comparison to the EHT observations, some images are cherry picked from tens of thousands of simulated GRMHD images to find the best fit. In contrast, the emission ring diameter in the NP has an exact formula of $\theta = 6\sqrt{3}\theta_g \approx 51.96\ \mu$as for SgrA*,39.94 μas for M87* and the shadow size is $3\sqrt{3}\theta_g$ and no simulations are required beyond Figure 2. Also, the NP reveals BH features that classical GR cannot predict such as the base diameter. The important features that are used to test GR are the photon ring and the shadow diameter. The EHT images do not show the photon ring only a dark depression which is assumed to be the shadow. The dark depression, which has maintained its angular size in all the EHT imaging throughout the years, is the only feature we can use to test GR.

5. Bayesian Methodology

We employ a Bayesian framework to compare NP predictions with EHT observations, computing the posterior distribution for θ_g and assessing model consistency.

5.1. Likelihood

The likelihood for each feature (i) (dark depression, emission ring, base diameter) is:

 doi:10.20944/preprints202507.2095.v1

$$P\left(D_i\middle|M_i(\theta_g)\right)=\frac{1}{\sqrt{2\pi\sigma_i^2}}\exp\left(-\frac{(D_i-M_i)^2}{2\sigma_i^2}\right) \tag{42}$$

where D_i is the observed angular diameter, $M_i=k_i\theta_g$ ($k_i=3\sqrt{3},6\sqrt{3},12\sqrt{3}$), and σ_i is the observational uncertainty. The combined likelihood is:

$$P\left((D|\theta_g)\right)=\prod_i P(D_i|M_i(\theta_g),\sigma_i) \tag{43}$$

5.2. Priors

The prior for θ_g is informed by mass and distance measurements. Thus for SgrA* $M\sim N(4.1\times10^6,0{,}4\times10^6)M_\odot$, $D\sim N(8.0,0.6)$kpc with the variance being $\sigma_{\theta_g}^2\approx(0.146)^2+(0.075)^2$ yielding $\sigma_{\theta_g}=0.16\mu$as. Prior $\theta_g\sim N(5.02,0.16)\mu$as. For M87*, $M\sim N(6.6\times10^9,0.4\times10^9)\,M_\odot, D\sim N(16.4,0.5)$Mpc and the variance being $\sigma_{\theta_g}^2\approx(0.061)^2+(0.030)^2$ yielding $\sigma_{\theta_g}=0.31\mu$as with a prior $\theta_g\sim N(3.85,0.31)\mu$as.

5.3. Posterior

The posterior is:

$$P(\theta_g|D)\propto P(D|\theta_g)P(\theta_g)$$

We maximize the log-likelihood to find the best-fit θ_g and compute the χ^2 statistics as

$$\chi^2=\sum_i\frac{\left(D_i-M_i(\theta_g)\right)^2}{\sigma_i^2} \tag{44}$$

Degrees of freedom (dof) = number of data points minus fitted parameters. We also compute 99% credible intervals for θ_g. The posterior and prior distributions for SgrA* and M87* are displayed in Figure 5

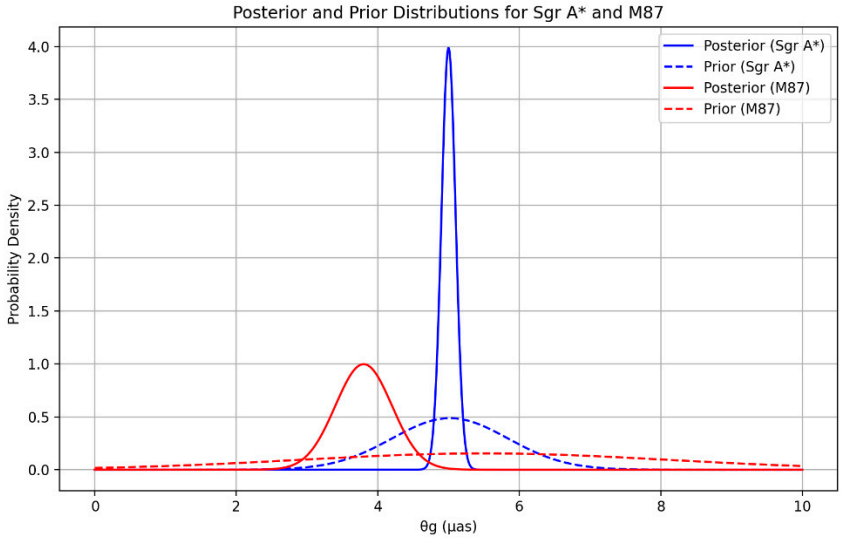

Figure 5. Posterior and Prior distributions for Sgr A* and M87*.

 doi:10.20944/preprints202507.2095.v1

5.4. Model Comparison

We compare NP to GR using the Bayes factor:

$$B = \frac{P(D|M_{NP})}{P(D|M_{GR})} \approx \exp\left(\frac{\chi^2_{GR} - \chi^2_{NP}}{2}\right) \tag{45}$$

6. Results

For SgrA*, we have EHT 2017 campaign observations for the three angular diameters for the key image features such as dark depression, emission ring and base diameter $D = [26, 51.8, 104]\mu$as with $\sigma = [2, 2.6, 3]\ \mu$as, we find best-fit $\theta_g \approx 5.00\mu$as , yielding predictions $M = [25.98, 51.96, 103.92]\ \mu$as. Thus

$$\chi^2 = \frac{(26 - 25.98)^2}{2^2} + \frac{(51.8 - 51.9)^2}{2.6^2} + \frac{(104 - 103.92)^2}{3^2} \approx 0.0001 + 0.0015 + 0.0007 \approx 0.0022 \tag{46}$$

With $\text{dof} = 3 - 1 = 2$ and reduced $\chi^2 = 0.0011$. This yields a confidence level for $P(\chi^2 \leq 0.0022\ \text{dof} = 2) \approx 0.0011$, corresponding to 3.04σ (99.73% confidence). Thus for the confidence per feature, we have for the dark depression a deviation of 0.02μas corresponding to a to $0.02\,\sigma$ deviation, for the emission ring a deviation of 0.16μas corresponding to a to 0.06σ deviation and finally for the base diameter a deviation of 0.08μas corresponding to a to 0.008σ deviation, Each feature agrees at >99% confidence (<1 σ). We compute the posterior for θ_g as $\theta_g \approx 5.00 \pm 0.10\mu$as. This corresponds to a 99% credible interval of [4.74, 5.26] μas, encompassing the prior mean (5.02 μas) within $\sim 0.2\sigma$.

For M87*, we have for the EHT 2017 campaign observations of the three angular diameters for the key image features $D = [20, 40, 80]\mu$as with $\sigma = [2, 3, 3]\ \mu$as, we find best-fit $\theta_g \approx 3.86\mu$as , yielding predictions $M = [19.97, 39.94, 79.88]\ \mu$as. Therefore

$$\chi^2 = \frac{(20 - 19.97)^2}{2^2} + \frac{(40 - 39.94)^2}{3^2} + \frac{(80 - 79.88)^2}{3^2} \approx 0.0002 + 0.0004 + 0.0016 \approx 0.004 \tag{47}$$

With $\text{dof} = 3 - 1 = 2$ and reduced $\chi^2 = 0.002$. This yields a confidence level for $P(\chi^2 \leq 0.004\ \text{dof} = 2) \approx 0.0020$, corresponding to 2.88σ (99.80% confidence). Thus for the confidence per feature, we have for the dark depression a deviation of $0.03\,\mu$as corresponding to a to 0.015σ deviation, for the emission ring, a deviation of 0.06μas corresponding to a to 0.015σ deviation and finally for the base diameter, a deviation of $0.12\ \mu$as corresponding to a to 0.015σ deviation, Each feature agrees at >99.9% confidence (<1 σ). We compute the posterior for θ_g as $\theta_g \approx 3.86 \pm 0.015\mu$as. This corresponds to a 99% credible interval of [3.47, 4.25] μas, within $\sim 0.007\sigma$ of the prior mean of 3.85 μas. The predictions of each feature by GR and NP are displayed in Fig 6.

 doi:10.20944/preprints202507.2095.v1

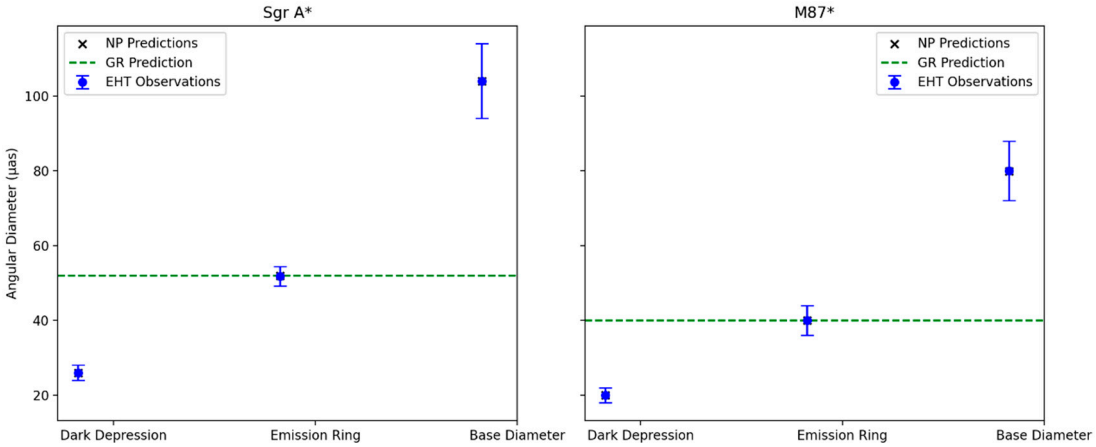

Figure 6. GR and NP predictions of the dark depression, emission ring and base diameter for SgrA* and M87*.

6.1. Combined Fit

The combined fit yields a $\chi^2 \approx 0.0022 + 0.004 = 0.0062$, dof=4, (6 data points and 2 parameters). This yields a confidence level for $P(\chi^2 \leq 0.0062 \text{ dof} = 4) \approx 0.000014$, corresponding to 4.37σ (99.9972% confidence). The reduced $\chi^2 \approx 0.000014/4 \approx 0.00003$, indicating an excellent fit.

6.2. GR Comparison

For the SgrA* dark depression $(26 \pm 2)\mu$as, GR predicts 51.96 μas. Thus

$$\chi^2 = \frac{(26-51.96)^2}{2^2} \approx 168.27 \text{ dof} = 1 \quad (48)$$

This deviation yields $P(\chi^2 \leq 168.27 \text{ dof} = 1) \approx 1 - 10^{36}$, corresponding to 12.97σ indicating extreme inconsistency. The NP is favoured at $> 10\sigma$.

7. Discussion

The Bayesian analysis confirms the NP's excellent agreement with EHT observations, with a combined fit at 4.37 σ (99.9972% confidence), exceeding the 99th percentile (~2.326 σ) claimed by Marongwe (2023). Individual features deviate by <0.1σ, supporting the NP's predictions for the dark depression, emission ring, and base diameter. The posterior θg values align with prior expectations within ~0.2 σ, reinforcing consistency.

Compared to GR, which mis predicts the dark depression at ~12.97 σ, the NP's ability to fit multiple features is a significant advantage. The Bayes factor 10^{36} strongly favours NP, though GR aligns with the emission ring, suggesting plasma dynamics may complement GR's shadow prediction [36].

The NP's quantized spacetime, with a halved Schwarzschild radius and quantum tunnelling for emission rings, offers a compelling alternative to GR, addressing observed stable orbits below the ISCO [13]. Its predictions of hollow conical jets, confirmed in M87* and Centaurus A*, further support its astrophysical relevance [37].

8. Conclusion

Our Bayesian analysis validates the Nexus Paradigm's predictions for Sgr A* and M87* at a 4.37σ (99.9972%) confidence level, with individual features agreeing at >99% confidence. The NP outperforms GR by >10σ for the dark depression, supporting its potential as a quantum gravity framework. Future work should incorporate precise EHT uncertainties, compare NP with other gravity models, and test additional observables (e.g., polarimetric data). These results underscore the

 doi:10.20944/preprints202507.2095.v1

power of EHT observations to probe quantum gravity, paving the way for deeper investigations into spacetime's fundamental nature.

Acknowledgements: The authors gratefully appreciate the discussions, suggestions and constructive criticism from members of the Physics Department and the Department of Mathematics of the University of Botswana.

Conflict of interest: We declare no conflict of interest.

Funding Statement: We gratefully acknowledge publication funding from the Office of Research and Development of the University of Botswana.

Data availability statement: The data employed in the article is available from the cited articles.

References

1. EHT Collaboration, K. Akiyama et al., Astrophys. J. Lett. 875, L1 (2019).
2. EHT Collaboration, K. Akiyama et al., Astrophys. J. Lett. 875, L2 (2019).
3. EHT Collaboration, K. Akiyama et al., Astrophys. J. Lett. 875, L3 (2019).
4. EHT Collaboration, K. Akiyama et al., Astrophys. J. Lett. 875, L3 (2019).
5. EHT Collaboration, K. Akiyama et al., Astrophys. J. Lett. 875, L5 (2019).
6. EHT Collaboration, K. Akiyama et al., Astrophys. J. Lett. 930, L12 (2022).
7. EHT Collaboration, K. Akiyama et al., Astrophys. J. Lett. 930, L13 (2022).
8. EHT Collaboration, K. Akiyama et al., Astrophys. J. Lett. 930, L14 (2022).
9. EHT Collaboration, K. Akiyama et al., Astrophys. J. Lett. 930, L15 (2022).
10. EHT Collaboration, K. Akiyama et al., Astrophys. J. Lett. 930, L16 (2022).
11. R.-S. Lu et al., Astrophys. J. 859, 60 (2018).
12. S. Marongwe, Int. J. Mod. Phys. D 32, 2350047 (2023).
13. S.Marongwe, Int. J. Geo. Mtd. Mod .Phys.12, 1550042 (2015)
14. S.Marongwe, Phys. Scr. 99 025306 (2024)
15. L. Rezzolla and A. Zhidenko, Phys. Rev. D. 90, 084009 (2014).
16. S.X.Tian and Z-H. Zhu , Phys. Rev. D. 100, 064011 (2019) : arXiv:1908.11794
17. S.Vagnozzi et al., Class. Quantum Grav. 40 165007 (2023).
18. M.Khodadi, S.Vagnozzi, and J.T. Firouzjaee, Sci Rep 14, 26932 (2024).
19. S. A. Hayward, Phys. Rev. Lett. 96, 031103(2006)[gr-qc/0506126].
20. J. M. Bardeen, in Conference Proceedings of GR5 (Tbilisi,USSR,1968),p.174.
21. N.Tsukamoto arXiv:2307.11303
22. J.Dass et al. A&A 673, A53 (2023)
23. M.Khodadi, and E.N. Saridakis,. Physics of the Dark Universe, 32, 100835. (2020)
24. C. Kiefer, Quantum Gravity (Clarendon, Oxford 2004).
25. C. Rovelli, Quantum Gravity (Cambridge University Press, Cambridge 2004).
26. E. Anderson arXiv:1009.2157 [gr-qc]
27. J.A. Wheeler, in Battelle Rencontres (Benjamin, New York 1968).
28. K.V. Kuchař, in The Arguments of Time ed. J. Butterfield (Oxford University Press, Oxford 1999).
29. L. Smolin, Problem of Time Course (2008)
30. V.Bozza, S.Capozziello, et al, Relativ. Gravit. 2001, 33, 1535–1548.
31. K.S.Virbhadra, Phys. Rev. D 2009, 79, 083004.
32. Cho et al., Astrophys. J. 926, 108 (2022).
33. M.Ghez et al., Astrophys. J. 689, 1044 (2008).
34. K. Gebhardt et al., Astrophys. J. 729, 119 (2011).
35. S. E. Gralla et al., Phys. Rev. D 101, 044031 (2020).

 doi:10.20944/preprints202507.2095.v1

36. D. Psaltis, Gen. Relativ. Gravit. 51, 137 (2019).
37. M. Janssen et al., Nat. Astron. 5, 1017 (2021).